The heterogeneity of dermal mesenchymal cells reproduced in skin equivalents regulates barrier function and elasticity

Shun Kimura[1*], Sachiko Sekiya[2, 3], Sawa Yamashiro[1], Tetsutaro Kikuchi[2], Masatoshi Haga[1], & Tatsuya Shimizu[2]

[1] *ROHTO Pharmaceutical Co., Ltd., Osaka, 544-8666, Japan*

[2] *Institute of Advanced Biomedical Engineering and Science, TWIns, Tokyo Women's Medical University, Tokyo, Japan*

[3] *Institute of Integrated Research Human Biology Research Unit, Institute of Science Tokyo, Tokyo, Japan*

*Correspondence to: skimura@rohto.co.jp

Manuscript information:

This manuscript comprises 56 pages of text, 6 figures, and 1 table.

Abstract

The heterogeneity of dermal mesenchymal cells, including perivascular mesenchymal cells and papillary and reticular fibroblasts, plays critical roles in skin homeostasis. Herein, we present human skin equivalents (HSEs), in which pericytes, papillary fibroblasts, and reticular fibroblasts are spatially organized through autonomous three-cell interactions among epidermal keratinocytes, dermal fibroblasts, and vascular endothelial cells. The replication of dermal mesenchymal cell heterogeneity enhances skin functions, including epithelialization, epidermal barrier formation, and dermal elasticity, enabling *in vitro* evaluation of drug efficacy using methodologies that are identical to those used in human clinical studies. Furthermore, ascorbic acid-induced epidermal turnover and synthesis of well-aligned extracellular matrix via perivascular niche cells play crucial roles in improving skin barrier function and elasticity. Therefore, HSEs with heterogeneous dermal mesenchymal cells may improve our understanding of the mechanisms underlying skin homeostasis through cell-to-cell communication and serve as a model to animal experiments for developing precision medicine.

Introduction

Intercellular crosstalk based on cellular heterogeneity plays a crucial role in maintaining the morphological and functional homeostasis of organs and has garnered attention as a potential target for studies on precision medicine[1]. Given that the integumentary organ system (IOS) is the most readily accessible organ system in the human body, the analysis of heterogeneity in human skin cells has established paradigms for scientific research in areas such as cell adhesion, inflammation, and tissue stem cells[2]. The IOS, which includes the skin, skin appendages, nerves, and blood vessels, plays essential roles in waterproofing, cushioning, protecting relatively deep tissues, excreting waste and thermoregulation[3]. Dermal mesenchymal cells contribute physical resilience by synthesizing extracellular matrix (ECM) components, such as collagen and elastin, and play a pivotal role in maintaining the homeostasis of epidermis, hair follicles, and vasculature structure via intercellular communication involving growth factors and cell adhesion[4,5]. Histological analyses and single-cell transcriptomes of the adult human skin have identified various subtypes of dermal mesenchymal cells, including papillary fibroblasts, reticular fibroblasts, pro-inflammatory fibroblasts, mesenchymal fibroblasts, dermal papilla cells, arrector pili muscle fibroblasts, pericytes, and mesenchymal stem cells[6–10]. The heterogeneity of dermal mesenchymal cells is modulated by factors, such

as age, anatomical location, both intrinsic and extrinsic stressors, thereby influencing physiological processes including wound healing, fibrosis, atopic dermatitis, and aging[11–13]. Interestingly, the potential for intervention in aberrant alterations of heterogeneity of dermal mesenchymal cell is being increasingly demonstrated, as exemplified by the suppression of ultraviolet-induced selective depletion of papillary fibroblasts through local cyclooxygenase 2 inhibition, and attenuation of aging-associated transcriptomic changes in dermal fibroblasts by caloric restriction[14,15]. Therefore, elucidating the functional characteristics of dermal mesenchymal cell subtypes and mechanisms that maintain homeostasis of the heterogeneity may significantly contribute to developing precision medical technologies targeting skin diseases and aging.

The identification and determination of functional characteristics of dermal mesenchymal cell heterogeneity have been conducted through *in vivo* studies in mice and humans. However, animal experimentation requires careful consideration of interspecies differences with humans and faces increasing societal demands for a reduction[16–19]. In contrast, human clinical studies are valuable for basic research and for validating efficacy; however, they are not suitable for large-scale screening of functional materials. To enable societal implementation dermal mesenchymal cell heterogeneity, developing *in vitro* research models that can replicate and assess dermal cellular heterogeneity and organ-

level functionality is necessary. Human cell-based *in vitro* research models such as two-dimensional (2D)-tissue cultured cells, skin organoids, and human skin equivalents (HSEs) are being explored as preclinical research tools for avoiding animal experimentation[20]. Although 2D tissue culture offers benefits for high-throughput screening, numerous subtypes of dermal mesenchymal cells, including papillary fibroblasts and pericytes, progressively lose their distinctive gene expression patterns and cellular morphology with successive passaging[7,21]. Spheroid culture-based organoids, which allow for sophisticated *in vitro* reconstruction of skin organ structures, including hair follicles, vasculature, and nerves, and the cellular heterogeneity of their constituent components, hold significant potential for advancing the understanding of cell–cell interactions and for future integration into drug screening platforms[22–25]. HSEs, distinguished by their capacity to fabricate tissues of customizable shapes at the centimeter scale, are already employed in the healthcare industry as commercially available platforms for tissue-level evaluation *in vitro*, encompassing drug safety, permeability, moisturizing barrier function, and mechanobiological aspects of skin physiology[26–28].

Basic HSEs, including those commercially available, comprise a fully stratified epidermal layer, along with a dermal equivalent formed from three-dimensional (3D)

ECM such as a decellularized dermis or a Type 1 collagen seeded with dermal fibroblasts [29,30]. The advancement of HSEs that relatively closely replicate the structure and functionality of native human skin is actively progressing by incorporating additional cell types, such as fibroblast subpopulations, vascular cells, immune cells, neural cells, and adipocytes, along with the integration of spheroid cultured tissues and application of 3D bioprinting technologies[31–33]. The vascular network, which is indispensable for delivering oxygen and nutrients and regulating of inflammatory responses, has been integrated into HSEs by incorporating vascular endothelial cells within the dermal compartment, transplanting endothelial cells into bioprinted vasculature-like structures, and implementing perfusion culture systems[34,35]. These innovations have facilitated the application of HSEs in drug delivery research[36]. Although the development of HSEs that reconstruct the cellular heterogeneity of native skin remains relatively limited, recent single-cell transcriptomic analyses have demonstrated that HSEs recapitulate the principal *in vivo* epidermal keratinocyte subtypes, and encompass unique keratinocyte populations exhibiting aberrant signaling pathways associated with epithelial–mesenchymal transition. Intriguingly, the appearance of these artificial cell subtypes is rescued by incorporating fibroblasts into dermal equivalents and xenografting onto immunodeficient mice, indicating that intercellular communication with keratinocytes

108 and dermal mesenchymal cells plays a crucial role in maintaining the homeostasis of
109 epidermal cell heterogeneity[37]. In contrast, the heterogeneity of dermal mesenchymal
110 cells of HSEs remains largely unexplored. To investigate the functional roles of distinct
111 dermal mesenchymal cell subpopulation, HSEs have been constructed using papillary
112 fibroblasts and pericytes derived from primary cultures of human dermis. These models
113 have revealed that epithelialization is strongly influenced by intercellular communication,
114 including Wnt signaling and laminin subunit alpha 5 (LAMA5)-mediated
115 pathways[7,21,38,39]. However, in constructing HSEs that replicate the heterogeneity of
116 dermal mesenchymal cells, the strategy for isolating, culturing, and spatially arranging
117 each cellular subpopulation is economically impractical.

118 In developing and regenerating different organs, cell-to-cell communication
119 plays an essential role in inducing and maintaining differentiation of constituent cells19.
120 A specific subset of tissue-resident mesenchymal cells located close to blood vessels plays
121 a key role in epidermal differentiation and ECM production4,40,41. Therefore, we
122 hypothesized that by vascularizing an HSE and reproducing cell-to-cell communication
123 on the basis of reconstructed perivascular niche, constructing an HSE that relatively
124 faithfully replicates the *in vivo* characteristics of skin would be possible. In this study, we
125 report an HSE that replicates the heterogeneity of human dermal mesenchymal cells,

126 including pericytes, papillary fibroblasts, and reticular fibroblasts, by utilizing
127 commercially available primary cells, specifically normal human epidermal keratinocytes
128 (NHEKs), normal human dermal fibroblasts (NHDFs), and human umbilical vein
129 endothelial cells (HUVECs). Additionally, we demonstrate that our HSEs serve as a
130 valuable model for elucidating the role of dermal mesenchymal cell heterogeneity in
131 preserving skin structural integrity and functional homeostasis.
132

Results

Tricellular communication among epidermal keratinocytes, dermal fibroblasts, and vascular endothelial cells enhances the organization of skin and blood vessels.

To investigate the role of communication among epidermal keratinocytes, dermal fibroblasts, and vascular endothelial cells in skin tissue formation, we reconstructed seven types of HSEs, each incorporating one to three types of these constituent cells. The HSEs were named using the initials of the incorporated cell types. Specifically, HSEs composed of a single cell type, epidermal keratinocytes, dermal fibroblasts, or vascular endothelial cells, were referred to as the E, D, or V models, respectively. Models containing two of these cell types were designated as the DV, EV, and ED models, and the model incorporating all three cell types was referred to as the EDV model (Fig. 1a and 1b). All HSEs were constructed using a previously reported method for reproducing tensional homeostasis in a skin model[27]. After 14 d of air lift culture, the reconstructed tissue was 12 mm in diameter and 1–2 mm in thickness. The E and EV models were transparent and extremely soft (Fig. 1b). Hematoxylin and eosin (H&E) staining was used to visualize the regulation of skin and blood vessel organization through cell-to-cell communication (Fig. 1c). In the E and EV models, an

151 abnormal epidermis lacking a basal cell layer formed, whereas normal epithelialization
152 was observed in the ED and EDV models. This finding indicates that crosstalk between
153 NHEKs and NHDFs is essential for epithelialization. Endothelial tubes in the dermis
154 were observed only sparsely in the V and EV models; however, they were distributed
155 throughout the skin in the DV and EDV models. In particular, the endothelial tubes in
156 the EDV model tended to orient horizontally along the skin surface and increased in
157 number with increasing distance from the epidermis. Sirius red staining revealed
158 localized collagen fiber deposition (Fig. 1d). In the ED model, collagen fiber formation
159 was confirmed at the epidermal–dermal junction because of the well-known interaction
160 between the epidermis and dermis. In the DV and EDV models, the distribution of
161 collagen deposition within the dermis was similar to that of the endothelial tubes.
162 Interestingly, collagen deposition at the epidermal–dermal junction and around
163 endothelial tubes was promoted in the EDV model compared to that in the ED and DV
164 models.

165 The morphogenesis of the epidermis, endothelial tube, and dermis in each HSE
166 was analyzed by using immunohistology. The results of epidermal marker staining
167 demonstrated that the epidermis of the ED and EDV models exhibited a cytokeratin 5
168 (CK5)-positive basal layer, a claudin 1 (CLDN1)-positive basal to granular layer,

169 filaggrin (FLG)-positive keratohyalin granules, and a cutokeratin 10 (CK10)-positive
170 stratum corneum, closely resembling the epidermis of natural human skin (Fig. 2a).
171 Furthermore, the number of Ki67-positive cells was highest in the EDV model and
172 relatively low in the ED, EV, and E models (Fig. 2b). Trans-epidermal water loss
173 (TEWL) in the EDV model was 9.68 g/m^2h, and water evaporation was significantly
174 suppressed compared to that in the ED model (Fig. 2c). These results indicate that
175 dermal fibroblast–epidermal keratinocyte communication, that promotes
176 epithelialization and barrier function is enhanced by vascular endothelial cells.

177 Immunostaining for the endothelial cell markers CD31 and von Willebrand
178 factor (vWF) revealed active endothelial tube formation in the presence of both
179 HUVECs and NHDFs (Fig. 2d). In the DV and EDV models, deposition of collagen
180 types 1 and 4 was observed around the endothelial tubes, suggesting fibroblast–
181 endothelial cell crosstalk stabilizes the endothelial tube structure through ECM synthesis
182 (Fig. 2d). In the ED model, formation of type 1 collagen fiber in the dermis was
183 stimulated around the epidermal–dermal junction, whereas in the EDV model, additional
184 strong type 1 collagen expression originating from endothelial tubes was observed,
185 resulting in the formation of collagen fibers that spread throughout the entire dermis.
186 Microcirculation in natural human skin is organized into horizontal plexuses situated 1–

187 1.5 mm below the skin surface[40]. Immunostaining for CD31 and type 1 collagen revealed
188 that the blood vessels and collagen fiber in the EDV model were distributed in parallel
189 to the epidermal plane, and mathematical assessment using 2D fast Fourier transform
190 (2D-FFT) analysis corroborated this observation (Fig. 2e). The collagen network, which
191 is arranged parallel to the skin surface, functions to withstand mechanical forces acting
192 perpendicular to the skin. Therefore, we evaluated the elasticity of HSEs, a physical
193 indicator of skin aging and correlating factor of wrinkles and sagging, using the
194 Cutometer-based protocol applied in human clinical studies[41]. Skin elasticity could be
195 measured only in the ED and EDV models because the tissue in the other HSEs was
196 damaged by negative pressure loading. The ED and EDV models withstood 10 negative
197 pressure loading cycles (Fig. 2f). The R7 value, which is an elasticity index reportedly
198 associated with facial sagging, increased in the EDV model (Fig. 2g).

199 Therefore, tricellular interactions among epidermal keratinocytes, dermal
200 fibroblasts, and endothelial cells play critical roles in epidermal turnover, collagen
201 synthesis, and angiogenesis and are sufficient to enhance tissue-scale skin functionality,
202 including viscoelastic properties, and integrity of the epidermal barrier.

203

204 **Cell-to-cell communication in a 3D environment replicates dermal mesenchymal**

205 **cell heterogeneity that is lost in 2D culture**

206 To evaluate the impact of vascularization on fibroblast heterogeneity in the HSEs,
207 we analyzed the spatial distribution of cells with positive markers for papillary fibroblasts
208 (CD39 and fibroblast activation protein [FAP]), reticular fibroblasts (CD36 and CD90),
209 and pericytes neural/glial antigen (NG2) and alpha-smooth muscle actin (αSMA) via
210 immunohistochemistry (Fig. 3a and 3b). Fibroblasts in the D model were positive for the
211 pan-fibroblast marker vimentin; however, the expression of all markers in papillary and
212 reticular fibroblasts and pericytes was barely detectable. CD39-positive cells were
213 observed in the DV and EDV models, and FAP-positive cells were observed in the ED
214 and EDV models. Interestingly, CD39-positive cells tended to localize around the
215 endothelial tubes, whereas FAP-positive cells were observed mainly near the epidermal–
216 dermal junction; similar patterns were also observed in natural human skin. CD36-
217 positive cells were distributed in the DV and EDV models, and CD90-positive cells were
218 sparsely distributed in the ED, and EDV models (Fig. 3a). NG2- and αSMA-positive
219 pericytes were localized to the periphery of the lumen formed by vWF-positive vascular
220 endothelial cells (Fig. 3b).

221 Immunohistochemical analysis revealed that the fibroblasts constituting the
222 HSEs exhibited heterogeneity in terms of expression of the cell surface markers,

223 depending on the constituent cell types. Therefore, we conducted single-cell RNA
224 sequencing (scRNA-seq) to analyze the single-cell transcriptomes of dermal
225 mesenchymal cell populations within the HSEs. We profiled three samples: the ED and
226 EDV models cultured at the air–liquid interface for 14 d, a mixture of NHEKs, NHDFs,
227 and HUVECs cultured separately under 2D conditions (referred to as 2D) (Fig. 4a). In an
228 initial analysis, we obtained an overview of diverse cell populations by integrating cells
229 from three samples. After quality filtering, a total of 23,911 cell profiles were successfully
230 obtained across all conditions. A uniform manifold approximation and projection
231 (UMAP) plot revealed three major cell populations and 20 distinct clusters (Fig. 4b, left).
232 Based on the existing marker genes, we identified four cell types (keratinocytes,
233 fibroblasts, vascular endothelial cells, and pericytes) for each cell culture (Fig. 4b, right).
234 The UMAP plot illustrates specific impact of each culture condition on fibroblast
235 population (Supplementary Fig. 1a). The major fibroblast clusters under 2D, #1, #6, #13,
236 and #17 were relatively minor subpopulations in the ED and EDV models. The clusters
237 #0, #2, #9, #10, and #11 were major in both the ED and EDV models; however, cluster
238 #14, characterized by the expression of pericyte marker genes (*ACTA2* and *RGS5*), was
239 detected as a subpopulation unique to the EDV model (Fig. 4c). We hypothesized that the
240 formation and maintenance of cluster #14 involves endothelial cell–fibroblast

241 communication and investigated this interaction using CellChat analysis[42]. Cluster #14
242 showed increased intracellular communication with vascular endothelial cell clusters
243 through vascular endothelial growth factor (VEGF)B–VEGF receptor 1 (VEGFR1),
244 placental growth factr (PGF)–VEGFR1, laminin–dystroglycan, and laminin–integrin
245 interactions compared to that by other fibroblasts clusters (Fig. 4d). The ED and EDV
246 models promoted the expression of collagen fiber-related genes such as *COL1A1*,
247 *COL3A1*, *COL4A1*, *COL4A2*, and *COL5A3*, but suppressed the expression of elastic
248 fiber-related genes, including *ELN* and *FBN1*, compared to that in the 2D conditions (Fig.
249 4e). This change in the transcriptome was relatively highly pronounced in the EDV model,
250 suggesting the contribution of cluster #14.

251 To investigate the biological significance of dermal mesenchymal cell
252 heterogeneity of the HSEs, we referred to a published *in vivo* human skin scRNA-seq
253 dataset and integrated it with our HSE datasets using the R Harmony data integration
254 algorithm[11]. A UMAP plot revealed four major cell populations and 11 distinct clusters
255 (Fig. 5a). To distinguish the results of this integrated analysis from previous *in vitro* data
256 analysis, apostrophes were added to the cluster numbers in this analysis. The four major
257 clusters were defined as keratinocytes, fibroblasts, vascular endothelial cells, and
258 pericytes according to the expression patterns of marker genes (Fig. 5b). In the ED and

259 EDV models, similar to *in vivo* skin, fibroblasts were composed of mainly clusters #0',
260 #1', and #8'. In contrast, 2D-cultured fibroblasts contained very few cells from clusters
261 #0' and #8', whereas clusters #2' and #11', which are rarely found in natural human skin,
262 comprised their main subpopulations (Fig. 5c). Cell cycle scoring using the Seurat
263 scRNA-seq analysis pipeline (ccSeurat)[43]
264 (https://satijalab.org/seurat/v3.1/cell_cycle_vignette.html) revealed that cells in cluster
265 #2', characteristic of 2D-cultured fibroblasts, were in the G2/M and S phases (Fig. 5d).
266 Four main fibroblast subpopulations that could be spatially localized and showed
267 differential secretory, mesenchymal and proinflammatory functional annotations have
268 been previously defined[11]. We reanalyzed this dataset for identifying these four fibroblast
269 subtypes and pericytes (Supplementary Fig. 2). We then plotted the cells corresponding
270 to each subtype on the integrated UMAP plot (Fig. 5e). Next, we analyzed the clustering
271 ratios within the integrated UMAP plot for each of the five natural human skin
272 subpopulations of cells including secretory papillary, secretory reticular, proinflammatory,
273 mesenchymal fibroblasts and pericytes (Fig. 5f). The results revealed that secretory
274 papillary and pro-inflammatory fibroblasts corresponded to cluster #0'; secretory
275 reticular fibroblasts corresponded to cluster #1'; mesenchymal fibroblasts corresponded
276 to cluster #8'; and pericytes corresponded to cluster #6'. We also investigated the Gene

277 Ontology (GO) terms enriched in cluster #0'; that represents the papillary fibroblast
278 phenotype and cluster #1'; that represents the reticular fibroblast phenotype. In cluster
279 #1'; GO terms related to collagen and elastic fiber formation were particularly enriched,
280 suggesting that cells in cluster #1' exhibited a phenotype closely resembling that of
281 reticular fibroblasts (Fig. 5g).
282

283 **Nutrient-poor culture conditions in the HSEs induce a senescent–like phenotype,**
284 **which is rescued by ascorbic acid**

285 Since blood vessels are central to maintaining organ homeostasis, vascular aging
286 is hypothesized to be a fundamental upstream factor of organismal aging[44,45]. During skin
287 aging, a reduction in blood vessels within the papillary layer and decline in their functions
288 are thought to contribute to thinning of the epidermis and papillary dermis owing to
289 impaired supply of nutrient and paracrine factors from vascular endothelial cells; however,
290 experimental evidence for this phenomenon remains limited[46–48]. Therefore, to evaluate
291 the impact of plasma-derived nutrient deprivation induced by peripheral vascular
292 reduction, ED and EDV were cultured for 10 d in a nutrient poor (NP) medium
293 characterized by low FBS concentration and lack of basic fibroblast growth factor (bFGF)
294 and ascorbic acid (AA). Moreover, ascorbic acid, a well-evaluated antiaging material

295 known for its antioxidant properties, ability to induce epithelialization, and role as a
296 coenzyme in collagen synthesis[49–51], was added to the NP medium for evaluating its
297 impact on HSE organization and skin functionality. H&E staining and
298 immunohistological analysis revealed that skin tissue, including the epidermis, dermis,
299 and endothelial tubes with pericytes, was reconstructed even under NP culture conditions
300 (Fig. 6a and 6b). However, the number of Ki67-positive cells in the epidermal basal cell
301 layer was significantly lower in the EDV model than in the ED model (Fig. 6c). When
302 500 μM AA was added, thickening of the CK5- and/or CK10- positive epidermal layer
303 and promotion of type 1 collagen deposition were observed in both the ED and EDV
304 models (Fig. 6b). AA increased the number of Ki67-positive cells in both the ED and
305 EDV models; however, the EDV model showed a significantly relatively high number in
306 the number of Ki67-positive cells (Fig. 6c). In both the ED and EDV models, ascorbic
307 acid reduced TEWL and enhanced skin barrier function (Fig. 6d). A 2D-FFT analysis
308 revealed that, NP culture conditions with AA resulted in horizontal orientation of CD31-
309 positive vascular endothelial cells and the surrounding type 1 collagen relative to the
310 epidermal layer, compared to that of the NP alone culture conditions (Fig. 6e).
311 Furthermore, in the AA-depleted EDV model, collagen fragments of types 3 and 4 were
312 deposited around CD31-positive endothelial tubes, suggesting collagen degradation (Fig.

313 6b). NG2- and αSMA-positive pericytes were observed surrounding the endothelial tubes
314 regardless of the presence or absence of AA (Fig. 6b). Although no changes were detected
315 in the ED model, skin elasticity was significantly increased by AA in the EDV model (Fig.
316 6f). In summary, NP culture conditions enabled *in vitro* replication of epidermal thinning,
317 barrier disruption, reduction in dermal elasticity with imbalanced collagen synthesis and
318 degradation, and disordered vascular orientation, characteristics similar to those of human
319 skin aging. AA was effective in mitigating these aging-related changes. These findings
320 demonstrate that our HSEs serve as a valuable tool for evaluating the efficacy of
321 functional molecules, and suggest that vascular endothelial cells and pericytes play
322 critical roles in the underlying mechanisms of action of these molecules.
323
324

Discussion

In this study, we demonstrated that the heterogeneity of dermal mesenchymal cells, such as papillary and reticular fibroblasts and pericytes, in natural human skin can be partially reproduced by reconstructing an HSE using NHEKs, NHDFs, and HUVECs. In particular, the EDV model containing a pericyte-like subpopulation significantly improved skin and vascular tissue structure, barrier function, and elasticity, enabling functional evaluation according to human clinical protocols. These results elucidate the role of vascular cells in the developing the heterogeneity of dermal mesenchymal cell and demonstrate that the incorporation of vasculature into HSEs is an effective approach for recapitulating nutrient supply and inflammatory responses, as traditionally considered, and achieving a relatively highly advanced reconstruction of the skin transcriptome and functional properties. Our HSE, which reproduces fibroblast heterogeneity using stably available primary culture cells, provides a model alternative to animal experiments, which can be used to analyze the mechanisms controlling skin physiological functions based on cell-to-cell communication.

Papillary fibroblasts play important roles in wound healing functions such as re-epithelialization and collagen synthesis. Furthermore, papillary fibroblasts derived from elderly donors have reduced ability of proliferation and low secretion levels of

343 keratinocyte growth factor, suggesting that this effect may involve loss of the papillary
344 dermis, and elasticity, and deformation of skin texture owing to aging[38,39]. In fact, recent
345 scRNA-seq analyses of human skin has revealed changes in fibroblast subpopulations in
346 the skin owing to aging and disease, suggesting the possibility of developing new
347 therapeutic strategies by controlling fibroblast heterogeneity[6,11,52]. Epidermal Wnt signals
348 are involved in inducing differentiation of the papillary fibroblast lineage, and
349 intervention in dermal fibroblast subpopulations controls skin morphogenesis and
350 functionality in animals[53]. However, owing to the lack of appropriate *in vitro* models and
351 ethical restrictions to clinical *in vivo* studies, the prospects of applying *in vitro* findings
352 of human fibroblast heterogeneity to *in vivo* health care are unclear. In our HSE,
353 fibroblasts induced by 3D culture were in the G1 phase and differentiated into papillary,
354 reticular, and mesenchymal fibroblast-like populations, exhibiting properties similar to
355 those of native skin fibroblasts. Interestingly, cells positive for FAP, a marker for papillary
356 fibroblasts, were present near the epidermal–dermal junction in both the ED and EDV
357 models; however, CD39-positive cells were observed only in the EDV model. This
358 observation suggests that the keratinocyte–fibroblast communication is required for the
359 induction and maintenance of papillary fibroblast differentiation, and that some
360 subpopulations, such as CD39-positive cells, may require interaction with vascular

361 endothelial cells. By elucidating the mechanisms controlling human fibroblast
362 heterogeneity via cell tracking and spatiotemporal gene expression control techniques,
363 our HSE may contribute to developing cell therapies for wound healing and aging.

364 In addition to papillary and reticular fibroblasts, perivascular mesenchymal cells,
365 such as dermal stem cells and pericytes, play important roles in skin morphogenesis and
366 function. Pericytes play an important role as the major source of ECM production during
367 tissue regeneration in severl organs[54,55]. HSEs reconstructed using human pericytes and
368 fibroblasts separated by flow cytometry have been reported to promote the proliferation
369 of epidermal basal cells through LAMA5 expression by pericytes[21]. In our EDV model,
370 epithelialization and dermal ECM synthesis were promoted with the emergence of a
371 pericyte-like population. However, our HSE is unique in that it does not require fresh
372 human skin and allows the construction of a model containing NG2- and αSMA-positive
373 pericytes in a relatively simple process using commercially available subcultured cells.
374 Pericytes are a heterogeneous cell population *in vivo*, and pericytes from the same tissue
375 may originate from multiple sources[56,57]. Integrative analysis of scRNA-seq data from
376 natural human skin and our HSEs revealed that although the pericyte-like population in
377 HSEs clustered with human pericytes within the same subpopulation, their distributions
378 on the UMAP plot only partially overlapped. At the very least, the induced pericyte-like

379 cluster #14 replicated well-known *in vivo* angiogenic processes through interactions with
380 endothelial cells, such as VEGFB and PGF signaling via VEGFR1, and basement
381 membrane-mediated interactions between laminins and integrins[58–60]. These results
382 suggest that the pericytes in our HSE partially replicate certain populations and functions
383 of human pericytes, although the origin of this cell lineage and mechanisms driving their
384 induction remain unclear. Cell tracking experiments using fluorescent dyes or genetic
385 modifications targeting HSE constituent cells may contribute to addressing these gaps.

386 In addition to replicating the heterogeneity of dermal mesenchymal cells, the
387 EDV model significantly improved dermal elasticity and skin barrier function. This
388 improvement in dermal elasticity is attributed to the functionality of active ECM synthesis
389 by pericytes, compared to that by other subpopulations, and the autonomous
390 recapitulation of oriented collagen fiber formation along endothelial tubes. Furthermore,
391 culturing under NP conditions enabled the HSE model to replicate the phenotype of aged
392 skin, including epidermal barrier dysfunction owing to reduced proliferation of basal
393 keratinocytes, diminished dermal elasticity owing to decreased collagen synthesis,
394 increased collagen degradation by matrix metalloproteinases, and loss of vascular
395 orientation. In natural human skin, oxidative stress and dermal ECM degradation cause
396 vascular atrophy and reduces vascular density, leading to depletion of nutrient and oxygen

397 supplies to the papillary dermis and epidermis, which contributes to aging. Our findings
398 support this hypothesis. In our NP HSEs, a reduction in vascular density was not observed,
399 which is likely attributed to VEGF in the medium continuously inducing angiogenesis.
400 AA, which functions as both an antioxidant and a coenzyme for 2-oxoglutarate-dependent
401 dioxygenases, is an effective skin–antiaging agent. However, the effects of AA on the
402 vascular endothelium and perivascular mesenchymal cells and its impact on skin
403 mechanical properties remain unclear. Our findings revealed that ascorbic acid increased
404 collagen synthesis in both the ED and EDV models but significantly improved skin
405 viscoelasticity only in the EDV model, indicating that vascular endothelial cells and
406 pericytes play crucial roles in regulating skin elasticity and serve as target cells for AA.
407 In summary, our model emphasizes the importance of vascular cells in the study of skin
408 aging.

409 In conclusion, we reconstructed HSEs that reproduced skin fibroblast
410 heterogeneity, tissue structure, and physiological function in natural human skin. Further
411 studies, such as elucidating the mechanisms controlling fibroblast heterogeneity,
412 evaluating the impact of each cell population on skin morphogenesis, and identifying
413 drugs that can control the decrease or increase in specific fibroblast populations, may
414 provide new insights into the fields of basic science, personalized medicine, and health

415 care. Our model may help avoid animal experiments and contribute to the sustainable
416 growth of the health care industry as a versatile tool for evaluating skin functionality as
417 an alternative to clinical research. HSEs that highly replicate skin cell heterogeneity and
418 function may be developed by improving their vascular structure through perfusion
419 culture and providing cell-to-cell communication via organoids such as the IOS and
420 nervous systems.
421

422 **Methods**

423

424 **Cell culture**

425 Normal human epidermal keratinocytes (NHEKs) were purchased from
426 KURABO Industries Ltd. (Osaka, Japan) and were maintained in HuMedia-KG2
427 (KURABO). Normal human dermal fibroblasts (NHDFs) were purchased from
428 KURABO and maintained in Dulbecco's modified Eagle's medium (Thermo Fisher
429 Scientific, MA, USA) supplemented with 10% fetal bovine serum (Corning, NY, USA),
430 100 units ml^{-1} penicillin, and 100 μg ml^{-1} streptomycin (Thermo Fisher Scientific).
431 Human umbilical vein endothelial cells (HUVECs) were purchased from KURABO and
432 maintained in HuMedia-EG2 (KURABO). All cells were seeded into 150-mm dishes and
433 grown in a humidified atmosphere of 5% CO_2 at 37 °C.

434

435 **Reconstruction of the tension homeostatic skin (THS) model**

436 The THS model was generated via the following procedure. A total of 24×10^5
437 NHDFs and 30×10^5 HUVECs were resuspended in 2.4 ml of 1.25 mg ml^{-1} bovine
438 dermis-derived native collagen solution (KOKEN CO. Ltd., Tokyo, Japan) that was
439 mixed with 1× DMEM (Thermo Fisher Scientific), 15 mM HEPES (Dojindo, Kumamoto,

440 Japan), 10 mM $NaHCO_3$ (FUJIFILM Wako Pure Chemical Corporation), and 5 mg ml^{-1}
441 fibrinogen from bovine plasma type I-S (Merck KGaA, Darmstadt, Germany); then, the
442 cells were plated in a high-density translucent-membrane cell culture insert (0.4-µm pore
443 size) (Corning, NY, USA) in 6-well plates. After solidification, the dermal equivalents
444 were held in place by a Snapwell culture insert (Corning). NHEKs were seeded at a
445 density of 1.1×10^6 cells/well on fixed dermal equivalents, and they were cultured in
446 growth medium under submersion conditions for 4 d in a humidified atmosphere at 37 °C
447 with 5% CO_2 and 12.5% O_2. After maintenance in a submersion culture, the HSEs were
448 exposed to the air-liquid interface in a humidified atmosphere at 37 °C with 5% CO_2. The
449 growth medium for culturing HSEs consisted of DMEM supplemented with 10% FBS,
450 1% penicillin/streptomycin, 5 µg ml^{-1} insulin (FUJIFILM Wako Pure Chemical
451 Corporation), 500 □M ascorbic acid (FUJIFILM Wako Pure Chemical Corporation), 10
452 ng ml^{-1} bFGF (PeproTech, NJ, USA), 1 µM hydrocortisone (FUJIFILM Wako Pure
453 Chemical Corporation), and 5 nM VEGF 165 Human Recombinant (PeproTech) and was
454 replaced with fresh medium every 48 to -72 h.
455
456 **H&E staining and immunohistochemistry**
457 For histological analysis, skin equivalents from three independent experiments

458 were fixed with 4% formaldehyde and embedded in paraffin or Tissue-Tek O.C.T.
459 compound (Sakura Finetek Japan Co., Ltd., Tokyo, Japan). Hematoxylin-eosin staining
460 was performed on paraffin sections (10 μm thick). The stained sections were observed
461 via AxioScan.Z1 (Carl Zeiss, Oberkochen, Germany). For fluorescence
462 immunohistochemistry, frozen sections (10 and 50 μm) and paraffin sections (10 μm)
463 were prepared and stained as previously described[23]. Details of the primary and secondary
464 antibodies and associated epitope recovery methods are included in Table 1. All
465 fluorescence microscopy images were captured with an AxioScan.Z1 or LSM 900
466 confocal microscope (Carl Zeiss).
467

468 **Quantitative analysis of epidermal cell proliferation.**

469 The proliferation rate of epidermal cells was quantified by counting
470 keratinocytes with Ki67-positive nuclei located at the basal or immediately suprabasal
471 epidermis. The measurement area was a total of 3 images obtained by randomly acquiring
472 three z-stack images of 1000 × 340 × 10 μm from HSE tissues that were derived from
473 three different wells.
474

475 **Quantification of blood vessel alignment**

476 Anisotropic alignment of endothelial tubes and collagen fibers was assessed via two-
477 dimensional fast Fourier transform (2D-FFT) analysis, as previously described[61]. Briefly,
478 uncompressed images of endothelial tubes labeled with anti-CD31 antibody and basement
479 membranes labeled with anti-COL1 antibody were analyzed with the FFT function of
480 ImageJ, and the radial summation of the FFT frequency plot was calculated via the Oval
481 profile plug-in. The degree of fiber alignment was reflected by the shape and height of
482 the major peak in the FFT alignment plot. Images with oriented blood vessels resulted in
483 a prominent peak centered at the principal axis of fiber alignment, whereas images with
484 unaligned actin fibers resulted in an alignment plot with a broad peak or no peak.
485

486 **Single-cell RNA-seq library preparation**

487 NHEKs, NHDFs, and HUVECs cultured to a subconfluent state were harvested
488 through trypsinization according to the product protocol. Briefly, the cells were washed
489 with HEPES-buffered solution (Kurabo) to remove the medium and treated with 0.025%
490 trypsin/EDTA solution (Kurabo) for 3–7 min, followed by the addition of a trypsin-
491 neutralizing solution (Kurabo) and centrifugation to obtain a cell pellet. Constituent HSE
492 cells were harvested through enzymatic digestion. On day 14 of air-liquid interface
493 culture, the epidermis and dermis of the HSE were mechanically separated using forceps.

494 The epidermal layer was enzymatically dissociated with 0.025% trypsin/EDTA solution,
495 while the dermal layer was incubated in 10% FBS-supplemented DMEM containing 5000
496 U/ml collagenase type 1 (Worthington Biochemical Corp., NJ, USA) in a 37 °C water
497 bath. The resulting cell suspension was filtered through a 70-µm cell strainer to remove
498 debris and centrifuged to obtain a cell pellet. Single-cell RNA sequencing was conducted
499 using the Chromium Next GEM Single Cell 3′ Kit v3.1, Chromium Next GEM Chip G
500 Single Cell Kit, and Dual Index Kit TT Set A (10x Genomics) according to the
501 manufacturer's protocol (CG000315 Rev E). Cell viability and count were assessed using
502 a Countess 3 Automated Cell Counter following trypan blue staining and visual inspection.
503 The cell suspension was processed on a chromium controller for gel bead-in-emulsion
504 (GEM) generation, where polyadenylated mRNA was reverse transcribed to cDNA and
505 uniquely barcoded. The cDNA was subjected to amplification, quality assessment via
506 electrophoresis, and library preparation involving fragmentation, end-repair, A-tailing,
507 adaptor ligation, and PCR amplification. Library quality was evaluated using Agilent's
508 High Sensitivity D5000 ScreenTape system, and the DNA concentration was measured
509 with a Qubit 1X dsDNA HS Assay Kit on a Qubit 4 Fluorometer. Libraries were
510 sequenced on an Illumina NovaSeq 6000 with PE150, generating approximately 120 Gb
511 of data per sample from ~800 million reads.

512

513 **Single-cell RNA-seq data processing: *In vitro* skin data**

514 FASTQ reads of 10× scRNA sequencing data were processed with the hg38
515 reference genome via Cell Ranger (v7.1.0)[62]. A total of 27,082 cells passed the quality
516 control steps. The processed matrices of different batches were merged, and the following
517 analyses were performed via SEURAT-1 (v5.0.3). Cells with 1,000 to 8,000 RNA features
518 and mitochondrial RNA contents of less than 7% were selected. The selected expression
519 matrix was normalized by the total number of UMIs per cell and was log-transformed.

520 The filtered dataset was split into original sample identities via the Split Object
521 function, followed by data log normalization of UMI counts and identification and the
522 identification of 2000 more variable genes per sample.

523 The integrated data were then used for standard cell clustering and visualization with
524 Seurat, which uses the 2000 most variable genes of the integrated dataset as input. Next,
525 we used the function FindIntegrationAnchors with default parameters and 30 canonical
526 correlation analysis (CCA) dimensions to identify the integration anchors between our
527 five datasets. These anchors were subsequently used for integration via the IntegrateData
528 function, again with the first 30 CCA dimensions and default parameters.

529 The integrated data were then used for standard cell clustering and visualization

530 with Seurat, which uses the 2000 most variable genes of the integrated dataset as input.
531 First, the data were scaled via the ScaleData function, and principal component analysis
532 (PCA) dimensions were calculated via the RunPCA function. Next, unsupervised
533 clustering of the data was performed with the FindNeighbors and FindClusters functions.
534 For the FindNeighbors function, we used the first 30 PCA dimensions to construct a
535 shared nearest neighbor (SNN) graph for our dataset. Then, we clustered the cells with
536 the function FindClusters via a shared nearest neighbor (SNN) modularity optimization-
537 based clustering algorithm with a resolution of 0.7. Finally, for visualization, we used the
538 RunUMAP function with default parameters and 30 PCA dimensions.
539

540 **Single-cell RNA-seq data processing: *In vivo* skin data and data integration with *in***
541 ***vitro* skin data**

542 *In vivo* skin single-cell analysis was carried out via methods described in
543 previous studies[11]. After mapping cell types based on the expression of marker genes for
544 each cell type, we further explored the correspondence between the clusters and the four
545 fibroblast subpopulations mentioned in the original paper. This was accomplished by
546 examining the expression of marker genes for papillary fibroblasts and reticular
547 fibroblasts, as well as the top enriched Gene Ontology (GO) terms for the four fibroblast

548 clusters. Consistent with previous studies, Cluster 1 was classified as secretory-reticular,
549 Cluster 2 as proinflammatory, Cluster 3 as secretory-papillary, and Cluster 9 as
550 mesenchymal.

551 To integrate *in vitro* and *in vivo* data, cells annotated as vascular ECs, pericytes,
552 keratinocytes, and fibroblasts were initially extracted from the *in vivo* dataset. The cells
553 from each sample were filtered under specific conditions: for *in vitro* samples, cells with
554 1000 to -8000 RNA features and mitochondrial RNA contents of less than 7% were
555 selected; for *in vivo* samples, the criteria were fewer than 7500 RNA features and
556 mitochondrial RNA contents of less than 5%. Following this, normalization was
557 performed via the SCTransform method. Using Seurat's default approach, the top 2000
558 genes with the most variability from each dataset were extracted. All the data were then
559 combined to compute principal component analysis (PCA) dimensions, and batch effects
560 between datasets were mitigated using the Harmony algorithm's RunHarmony unction
561 (parameters set to theta=1, max.iter.harmony=10). Unsupervised clustering of the data
562 was subsequently performed via the FindNeighbors and FindClusters functions. Finally,
563 for visualization purposes, the RunUMAP function was employed with default
564 parameters and 30 PCA dimensions.

565

566 **Cell–to-cell communication analysis**

567 To analyze the estimated intercellular interactions established by different cell
568 types present in artificial skin, we utilized R CellChat3 (v1.6.1)[63]. This tool can
569 quantitatively infer and analyze intercellular communication networks from scRNA-seq
570 data and contains ligand-receptor interaction databases (http://www.cellchat.org/). In our
571 approach, pairwise comparisons across all cell clusters present in the artificial skin dataset
572 were conducted, and the analysis was performed using the default parameters set by the
573 tool.

574

575 **Evaluation of the epidermal barrier function of HSEs via TEWL measurement**

576 Trans-epidermal water loss (TEWL) was measured in the HSEs (n = 4) using a
577 Tewameter TM HEX (Courage & Khazaka electronic, Cologne, Germany) according to
578 the instruction manual. Prior to collection, the skin equivalent was incubated inside the
579 biosafety cabinet for 15 min to allow equilibration to the ambient temperature and
580 humidity of the room. The measurement was repeated three times, and the average and
581 standard deviation of each well were calculated.

582

583 **Measurements of skin elasticity**

584 Skin elasticity was determined via a noninvasive, *in vivo* suction skin elasticity
585 meter, the Cutometer MPA 580 (Courage & Khazaka electronic). The measurement
586 conditions were the same as those used in previously reported human clinical studies[41].
587 Briefly, with a 2-mm probe, a negative pressure of 400 mbar was applied to the HSEs for
588 a period of 2 s, followed by 2 s of relaxation time, and the ratio of immediate retraction
589 (Ur) and the ability of redeformation of the skin (Ua) to final distension (Uf) was analyzed
590 (R2 = Ua/Uf, R7 = Ur/Uf).
591

592 **Nutrient-poor culture of HSEs and evaluation of their responsiveness to ascorbic**
593 **acid**

594 All HSEs were treated with nutrient-poor medium (DMEM supplemented with
595 1% FBS, 1% penicillin/streptomycin, 5 μg ml^{-1} insulin, and 1 μM hydrocortisone) at the
596 air-liquid interface on day 3 and maintained for 12 d. Then, 500 μM ascorbic acid was
597 added to the HSEs cultured at the air-liquid interface on day 5 and maintained for 10 d.
598

599 **Statistics and reproducibility**

600 Microsoft Excel (Microsoft, Redmond, WA, USA) and BellCurve for Excel
601 were used for statistical analysis. All values are expressed as the means ± standard

602 deviations (SDs). Analysis of the samples was performed at least in triplicate, and the

603 results were averaged. Differences between groups were considered significant at

604 $P<0.05$. All the experiments were repeated at least two times.

605

606 **Data availability**

607 scRNA-seq data from this study have been deposited into the Sequence Read
608 Archive (SRA) database under the BioProject ID. PRJNA1191968. All data are
609 available from the corresponding authors upon reasonable request.

610

611 **References**

612 1. Cha, J. & Lee, I. Single-cell network biology for resolving cellular
613 heterogeneity in human diseases. *Exp Mol Med* **52**, 1798–1808 (2020).
614 2. Watt, F. M. Mammalian skin cell biology: At the interface between
615 laboratory and clinic. *Science (1979)* **346**, 937–940 (2014).
616 3. Jiang, T.-X. *et al.* Integument pattern formation involves genetic and
617 epigenetic controls: feather arrays simulated by digital hormone models
618 HHS Public Access. *Int J Dev Biol* **48**, 117–135 (2004).
619 4. Di Carlo, S. E. & Peduto, L. The perivascular origin of pathological
620 fibroblasts. *Journal of Clinical Investigation* vol. 128 54–63 Preprint at
621 https://doi.org/10.1172/JCI93558 (2018).
622 5. Ganier, C., Rognoni, E., Goss, G., Lynch, M. & Watt, F. M. Fibroblast
623 Heterogeneity in Healthy and Wounded Skin. *Cold Spring Harb*
624 *Perspect Biol* a041238 (2022) doi:10.1101/cshperspect.a041238.
625 6. Tabib, T., Morse, C., Wang, T., Chen, W. & Lafyatis, R. SFRP2/DPP4 and
626 FMO1/LSP1 Define Major Fibroblast Populations in Human Skin.
627 *Journal of Investigative Dermatology* **138**, 802–810 (2018).
628 7. Philippeos, C. *et al.* Spatial and Single-Cell Transcriptional Profiling

Identifies Functionally Distinct Human Dermal Fibroblast Subpopulations. *Journal of Investigative Dermatology* **138**, 811–825 (2018).

8. Vorstandlechner, V. *et al.* Deciphering the functional heterogeneity of skin fibroblasts using single-cell RNA sequencing. *The FASEB Journal* **34**, 3677–3692 (2020).

9. Ascensión, A. M., Fuertes-Álvarez, S., Ibañez-Solé, O., Izeta, A. & Araúzo-Bravo, M. J. Human Dermal Fibroblast Subpopulations Are Conserved across Single-Cell RNA Sequencing Studies. *Journal of Investigative Dermatology* **141**, 1735-1744.e35 (2021).

10. Bensa, T., Tekkela, S. & Rognoni, E. Skin fibroblast functional heterogeneity in health and disease. *J Pathol* **260**, 609–620 (2023).

11. Solé-Boldo, L. *et al.* Single-cell transcriptomes of the human skin reveal age-related loss of fibroblast priming. *Commun Biol* **3**, 1–12 (2020).

12. Reynolds, G. *et al.* Developmental cell programs are co-opted in inflammatory skin disease. *Science (1979)* **371**, (2021).

13. He, H. *et al.* Single-cell transcriptome analysis of human skin identifies novel fibroblast subpopulation and enrichment of immune subsets in

647 atopic dermatitis. *Journal of Allergy and Clinical Immunology* **145**,
648 1615–1628 (2020).
649 14. Ma, S. *et al.* Caloric Restriction Reprograms the Single-Cell
650 Transcriptional Landscape of Rattus Norvegicus Aging. *Cell* **180**, 984-
651 1001.e22 (2020).
652 15. Salzer, M. C. *et al.* Identity Noise and Adipogenic Traits Characterize
653 Dermal Fibroblast Aging. *Cell* **175**, 1575-1590.e22 (2018).
654 16. Bassi, G., Grimaudo, M. A., Panseri, S. & Montesi, M. Advanced multi-
655 dimensional cellular models as emerging reality to reproduce In Vitro
656 the human body complexity. *International Journal of Molecular*
657 *Sciences* vol. 22 1–28 Preprint at https://doi.org/10.3390/ijms22031195
658 (2021).
659 17. Ferreira, M., Matos, A., Couras, A., Marto, J. & Ribeiro, H. Overview of
660 Cosmetic Regulatory Frameworks around the World. *Cosmetics* vol. 9
661 Preprint at https://doi.org/10.3390/cosmetics9040072 (2022).
662 18. Voelkl, B. *et al.* Reproducibility of animal research in light of biological
663 variation. *Nature Reviews Neuroscience* vol. 21 384–393 Preprint at
664 https://doi.org/10.1038/s41583-020-0313-3 (2020).

665 19. Lynch, M. D. & Watt, F. M. Fibroblast heterogeneity: implications for
666 human disease. *Journal of Clinical Investigation* **128**, 26–35 (2018).
667 20. Marx, V. Closing in on cancer heterogeneity with organoids. *Nat*
668 *Methods* **21**, 551–554 (2024).
669 21. Paquet-Fifield, S. *et al.* A role for pericytes as microenvironmental
670 regulators of human skin tissue regeneration. *Journal of Clinical*
671 *Investigation* **119**, 2795–2806 (2009).
672 22. Hong, Z. X. *et al.* Bioengineered skin organoids: from development to
673 applications. *Mil Med Res* **10**, 1–17 (2023).
674 23. Toyoshima, K. E. *et al.* Fully functional hair follicle regeneration
675 through the rearrangement of stem cells and their niches. *Nat Commun*
676 **3**, (2012).
677 24. Ibrahim, M. & Richardson, M. K. Beyond organoids: In vitro
678 vasculogenesis and angiogenesis using cells from mammals and
679 zebrafish. *Reproductive Toxicology* **73**, 292–311 (2017).
680 25. Nebuloni, F., Morgan, J., Walsh, E. J. & Cook, P. R. A platform for
681 modular assembly and feeding of micro-organoids on standard Petri
682 dishes. *Biol Open* **12**, (2023).

683 26. Ali, N. *et al.* Skin equivalents: skin from reconstructions as models to
684 study skin development and diseases. *British Journal of Dermatology*
685 **173**, 391–403 (2015).
686 27. Kimura, S. *et al.* Tissue-scale tensional homeostasis in skin regulates
687 structure and physiological function. *Commun Biol* **3**, (2020).
688 28. Bouwstra, J. A., Helder, R. W. J. & El Ghalbzouri, A. Human skin
689 equivalents: Impaired barrier function in relation to the lipid and
690 protein properties of the stratum corneum. *Adv Drug Deliv Rev* **175**,
691 113802 (2021).
692 29. Bell, E., Ivarsson, B. & Merrill, C. Production of a tissue-like structure
693 by contraction of collagen lattices by human fibroblasts of different
694 proliferative potential in vitro. *Proceedings of the National Academy of*
695 *Sciences* **76**, 1274–1278 (1979).
696 30. Nusgens, B., Merrill, C., Lapiere, C. & Bell, E. Collagen biosynthesis by
697 cells in a tissue equivalent matrix in vitro. *Coll Relat Res* **4**, 351–63
698 (1984).
699 31. Hofmann, E., Schwarz, A., Fink, J., Kamolz, L. P. & Kotzbeck, P.
700 Modelling the Complexity of Human Skin In Vitro. *Biomedicines* **11**, 1–

701 17 (2023).

702 32. Hosseini, M., Koehler, K. R. & Shafiee, A. Biofabrication of Human Skin
703 with Its Appendages. *Adv Healthc Mater* **11**, (2022).

704 33. Weng, T. *et al.* 3D bioprinting for skin tissue engineering: Current
705 status and perspectives. *J Tissue Eng* **12**, (2021).

706 34. Ponec, M. *et al.* Endothelial network formed with human dermal
707 microvascular endothelial cells in autologous multicellular skin
708 substitutes. *Angiogenesis* **7**, 295–305 (2004).

709 35. Black, A. F., Berthod, F., L'Heureux, N., Germain, L. & Auger, F. A. *In*
710 *vitro* reconstruction of a human capillary-like network in a tissue-
711 engineered skin equivalent. *The FASEB Journal* **12**, 1331–1340 (1998).

712 36. Abaci, H. E. *et al.* Human Skin Constructs with Spatially Controlled
713 Vasculature Using Primary and iPSC-Derived Endothelial Cells. *Adv*
714 *Healthc Mater* **5**, 1800–1807 (2016).

715 37. Stabell, A. R. *et al.* Single-cell transcriptomics of human-skin-
716 equivalent organoids. *Cell Rep* **42**, (2023).

717 38. Sriram, G., Bigliardi, P. L. & Bigliardi-Qi, M. Fibroblast heterogeneity
718 and its implications for engineering organotypic skin models in vitro.

Eur J Cell Biol **94**, 483–512 (2015).

39. Mine, S., Fortunel, N. O., Pageon, H. & Asselineau, D. Aging alters functionally human dermal papillary fibroblasts but not reticular fibroblasts: A new view of skin morphogenesis and aging. *PLoS One* **3**, (2008).

40. Braverman, I. M. The cutaneous microcirculation. *Journal of Investigative Dermatology Symposium Proceedings* **5**, 3–9 (2000).

41. Ezure, T., Hosoi, J., Amano, S. & Tsuchiya, T. Sagging of the cheek is related to skin elasticity, fat mass and mimetic muscle function. *Skin Research and Technology* **15**, 299–305 (2009).

42. Jin, S., Plikus, M. V. & Nie, Q. CellChat for systematic analysis of cell–cell communication from single-cell transcriptomics. *Nat Protoc* (2024) doi:10.1038/s41596-024-01045-4.

43. Butler, A., Hoffman, P., Smibert, P., Papalexi, E. & Satija, R. Integrating single-cell transcriptomic data across different conditions, technologies, and species. *Nat Biotechnol* **36**, 411–420 (2018).

44. Rastogi, C. *et al.* Counteracting age-related VEGF signaling insufficiency promotes healthy aging and extends life span. *Science*

(1979) **373**, E3692–E3701 (2021).

45. Le Couteur, D. G. & Lakatta, E. G. A Vascular Theory of Aging. *J Gerontol A Biol Sci Med Sci* **65A**, 1025–1027 (2010).

46. Bonta, M., Daina, L. & Muțiu, G. The process of ageing reflected by histological changes in the skin. *Rom J Morphol Embryol* **54**, 797–804 (2013).

47. Braverman, I. M. & Keh-Yen, A. Ultrastructure of the Human Dermal Microcirculation. III. The Vessels in the Mid- and Lower Dermis and Subcutaneous Fat. *Journal of Investigative Dermatology* **77**, 297–304 (1981).

48. Gunin, A. G., Petrov, V. V., Vasilieva, O. V. & Golubtsova, N. N. Age-related changes of blood vessels in the human dermis. *Advances in Gerontology* **5**, 65–71 (2015).

49. Masaki, H. Role of antioxidants in the skin: Anti-aging effects. *J Dermatol Sci* **58**, 85–90 (2010).

50. Boo, Y. C. Ascorbic Acid (Vitamin C) as a Cosmeceutical to Increase Dermal Collagen for Skin Antiaging Purposes: Emerging Combination Therapies. *Antioxidants* **11**, (2022).

755 51. Pullar, J. M., Carr, A. C. & Vissers, M. C. M. The roles of vitamin C in
756 skin health. *Nutrients* **9**, (2017).
757 52. He, H. *et al.* Single-cell transcriptome analysis of human skin identifies
758 novel fibroblast subpopulation and enrichment of immune subsets in
759 atopic dermatitis. *Journal of Allergy and Clinical Immunology* **145**,
760 1615–1628 (2020).
761 53. Driskell, R. R. *et al.* Distinct fibroblast lineages determine dermal
762 architecture in skin development and repair. *Nature* **504**, 277–281
763 (2013).
764 54. Kramann, R. *et al.* Perivascular Gli1+ progenitors are key contributors
765 to injury-induced organ fibrosis. *Cell Stem Cell* **16**, 51–66 (2015).
766 55. Greenhalgh, S. N., Iredale, J. P. & Henderson, N. C. Origins of fibrosis:
767 Pericytes take centre stage. *F1000Prime Rep* **5**, (2013).
768 56. Dias Moura Prazeres, P. H. *et al.* Pericytes are heterogeneous in their
769 origin within the same tissue. *Developmental Biology* vol. 427 6–11
770 Preprint at https://doi.org/10.1016/j.ydbio.2017.05.001 (2017).
771 57. Goss, G., Rognoni, E., Salameti, V. & Watt, F. M. Distinct Fibroblast
772 Lineages Give Rise to NG2+ Pericyte Populations in Mouse Skin

Development and Repair. *Front Cell Dev Biol* **9**, 1–18 (2021).

58. Greenberg, J. I. *et al.* A role for VEGF as a negative regulator of pericyte function and vessel maturation. *Nature* **456**, 809–814 (2008).

59. Huang, H. Pericyte-endothelial interactions in the retinal microvasculature. *International Journal of Molecular Sciences* vol. 21 1–18 Preprint at https://doi.org/10.3390/ijms21197413 (2020).

60. Bergers, G. & Song, S. The role of pericytes in blood-vessel formation and maintenance. *Neuro-Oncology* vol. 7 452–464 Preprint at https://doi.org/10.1215/S1152851705000232 (2005).

61. Aw, W. Y., Heck, B. W., Joyce, B. & Devenport, D. Transient Tissue-Scale Deformation Coordinates Alignment of Planar Cell Polarity Junctions in the Mammalian Skin. *Current Biology* **26**, 2090–2100 (2016).

62. Hao, Y. *et al.* Dictionary learning for integrative, multimodal and scalable single-cell analysis. *Nat Biotechnol* **42**, 293–304 (2024).

63. Jin, S. *et al.* Inference and analysis of cell-cell communication using CellChat. *Nat Commun* **12**, 1–20 (2021).

Acknowledgments: We thank laboratory members at the Institute of Advanced Biomedical Engineering and Science, TWIns, Tokyo Women's Medical University. We also thank Mr. M. Hashimoto, Y. Hayashi, and all the members of Rohto Pharmaceutical Co., Ltd., for their support and encouragement in this project. We would like to thank Rohto Pharmaceutical Co., Ltd., for funding support.

Author contributions: S.K., S.S. and T.S. designed the research plans; S.K. and S.Y. performed the experiments; S.K., S.S., T.K., S.Y., M.H., and T.S. discussed the results; and S.K. and S.Y. wrote the manuscript.

Competing interests: S.K., S.Y., and M.H. are employees of Rohto Pharmaceutical Co., Ltd.. T.S., S.S, and T.K have collaborated with Rohto Pharmaceutical Co., Ltd. and received research funding from the company. A part of the study was financially supported by Rohto Pharmaceutical Co., Ltd. under a collaboration contract with Tokyo Women's Medical University.

Author information: Correspondence and requests for materials should be addressed to S.K. (skimura@rohto.co.jp).

809

810 **Figure Legends**

811 **Figure 1 Tricellular communication regulates skin and vascular organization.**

812 (a) Schematic of the construction method of HSEs. (b) Macroscopic images of the

813 HSEs. Scale bar, 1 mm. (c) H&E-stained images of human skin and the HSEs at low

814 (upper columns; scale bar, 200 μm) and high (lower columns; scale bar, 50 μm)

815 magnification. The arrowheads indicate the endothelial tube. (d) Sirius red-stained

816 images of human skin and the HSEs; scale bar, 50 μm.

817

818 **Figure 2 Tricellular communication enhances skin barrier function and elasticity**

819 **by inducing self-organization.**

820 (a) Immunohistochemical analyses of human skin and the HSEs for evaluating

821 epithelialization. The dotted lines indicate the boundary between the epidermis and

822 dermis. Scale bar, 50 μm. (b) Analysis of the Ki67-positive basal keratinocyte ratio in

823 HSEs. *$P < 0.001$ (Dunnett's test following two-way analysis of variance). (c) TEWL

824 analysis of the ED and EDV models *$P < 0.05$ (two-tailed Student's t–tests; error bars

825 represent standard deviation). (d) Immunohistochemical analyses of human skin and

826 HSEs for evaluating angiogenesis and dermal collagen synthesis. (e) Macroscopic

827 image of CD31 and COL1 distribution (upper column) and FFT analysis (lower

828 columns) of the alignment of CD31-positive endothelial tubes and COL1-positive type
829 1 collagen fibers in the EDV model. Scale bar, 500 μm. (f) Skin deformation curves of
830 the ED (upper panel) and EDV models (lower panel). (g) Evaluation of R7 factors of the
831 ED and EDV models. *P < 0.05 (two-tailed Student's t-tests; error bars represent
832 standard deviation).
833
834 **Figure 3. Immunohistological analysis of dermal mesenchymal cell distribution in**
835 **the HSEs and human skin**
836 (a) Immunohistochemical analyses of ED, EDV and human skin samples to evaluate the
837 presence and distribution of dermal mesenchymal cell subpopulations. Scale bar, 50
838 μm. (b) Immunohistochemical analysis of pericyte distribution in ED, EDV, and human
839 skin tissues. Scale bar, 50 μm.
840
841 **Figure 4. The 3D culture environment and cell-to-cell communication replicate**
842 **dermal mesenchymal cell heterogeneity *in vitro.***
843 (a) Illustration of the workflow for sampling and analysis of the scRNA-seq data. (b)
844 UMAP plot of the scRNA-seq data for in *vitro* HSEs; the average expression of four
845 cell-type markers projected onto the UMAP plot for identifing cell populations. (c)

846 Distribution of fibroblasts and pericytes under each of the three conditions. (d) Cellular
847 communication from vascular endothelial cells (ECs; Clusters #4 and #5) to pericytes in
848 Cluster #14 and fibroblasts in Cluster #9. (e) Heatmap showing the average expression
849 of ECM-related genes across all fibroblasts under different conditions.
850
851 **Figure 5 Biological significance of fibroblast heterogeneity in HSEs through**
852 **integrated analysis of human scRNA-seq data.**
853 (a) UMAP plot of the scRNA-seq data for integrating HSEs and *in vivo* skin data. (b)
854 Average expression of established cell type markers was projected on the UMAP plot to
855 identify cell populations. Red indicates maximum gene expression, whereas blue
856 indicates low or no expression of a particular set of genes in log-normalized UMI
857 counts. (c) UMAP plot integrating the scRNA-seq data of HSEs and *in vivo* skin,
858 showing the distribution of fibroblasts and pericytes across the three *in vitro* and *in vivo*
859 conditions. (d) Cell cycle status of fibroblasts under each condition. (e) UMAP plot
860 showing the correspondence of the four fibroblast subpopulations and pericytes, as
861 previously reported[11]. (f) Proportion of cells from each subpopulation as previously
862 defined[11] and their clustering into specific clusters, as shown in Fig. 4e. (g) Enriched
863 GO terms in clusters #0' and #1'.

Figure 6 NP culture conditions in the HSEs induce a senescent phenotype, which is suppressed by AA.

(a) H&E-stained images of skin tissue organization induced by AA supplementation in the HSEs cultured under NP conditions. Scale bar, 100 μm. (b) Immunohistochemical analysis of the HSEs for visualizing the impact of NP conditions and ascorbic acid on re-epithelialization, dermal ECM synthesis, and angiogenesis. Scale bar, 50 μm. (c) Analysis of the Ki67-positive basal keratinocyte ratio in the HSEs. *$P < 0.001$ (two-tailed Student's t-tests; error bars represent standard deviation). (d) TEWL analysis of the ED and EDV models. *$P < 0.001$ (two-tailed Student's t-tests; error bars represent standard deviation). (e) A 2D-FFT analysis (lower columns) of the alignment of CD31-positive endothelial tubes and COL1-positive type 1 collagen fibers in the EDV model. (f) Evaluation of R7 factors of the ED and EDV models. *$P < 0.01$ (two-tailed Student's t-tests; error bars represent standard deviation).

879 **Supplementary Information**

880 **Supplementary Figure 1. scRNA-seq analysis of all *in vitro* samples.**

881 UMAP plot of scRNA-seq for *in vitro* human skin data, and distribution of all cells

882 under each of the three conditions (2D, 3D_ED, and 3D_EDV).

883

884 **Supplementary Figure 2. Re-evaluation of *in vivo* samples through scRNA-seq**.

885 (a) A UMAP plot presenting single-cell transcriptomic data from whole human skin

886 samples (n = 5). Each point signifies a single cell, with coloration based on

887 unsupervised clustering executed using Seurat. (b) Mean expression of genes forming

888 the papillary and reticular gene signatures applied to predict the dermal localization of

889 fibroblasts within the four clusters. (c) The 10 top significantly enriched GO terms

890 within each fibroblast subpopulation, arranged by *P*-value (d) A UMAP plot featuring

891 the average expression of previously established cell type markers for distinguishing

892 cell populations. Red denotes maximum gene expression, whereas blue represents

893 minimal or non-existent expression of a specific gene set in log-normalized UMI

894 counts.

895

896 Table 1. **Primary and secondary antibodies.**

Antibodies	**Source**	**Cat#**	**Dilution ratio**
Primary			
Anti-Cytokeratin 5 antibody	Abcam	Ab52635	1/200
Anti-Cytokeratin 10 antibody	Abcam	Ab9026	1/200
Anti-Claudin 1 antibody	Abcam	ab211737	1/250
Filaggrin Monoclonal Antibody (FLG01)	Thermo Fisher Scientific	MA5-13440	1/50
Anti-Ki67 antibody	Abcam	ab156956	1/150
Anti-Collagen I antibody	Abcam	ab34710	1/200
Anti-Collagen IV antibody	Abcam	ab6311	1/250
Anti-CD31 antibody	Abcam	ab9498	1/1000
Anti-CD31 antibody	Abcam	ab28364	1/50
Anti-Von Willebrand Factor antibody	Abcam	ab778	1/50
anti-Collagen Type 1 (3/4 fragment), pAb	AdipoGen	AG-25T-0113	1/50
Anti-alpha smooth muscle Actin	Abcam	ab5694	1/100
Anti-NG2 antibody	Abcam	ab139406	1/250
Anti-Fibroblast activation protein, alpha antibody	Abcam	ab207178	1/250

Anti-CD36 antibody	Abcam	ab252923	1/250
Anti-CD39 antibody	Abcam	ab223842	1/1000
Anti-CD90 / Thy1 antibody	Abcam	ab92574	1/200
Anti-Vimentin antibody	Abcam	ab8978	1/500
Secondary			
Alexa Fluor® 594 donkey anti-rabbit IgG	Thermo Fisher Scientific	A21207	1/500
Alexa Fluor® 594 donkey anti-mouse IgG (H + L) antibody	Thermo Fisher Scientific	A21203	1/500
Alexa Fluor® 488 donkey anti-rabbit IgG (H + L)	Thermo Fisher Scientific	A21206	1/500
Alexa Fluor® 488 donkey anti-mouse IgG (H + L)	Thermo Fisher Scientific	A21202	1/500

897 The table shows the commercially available antibodies which were used for

898 immunohistochemical analyses.

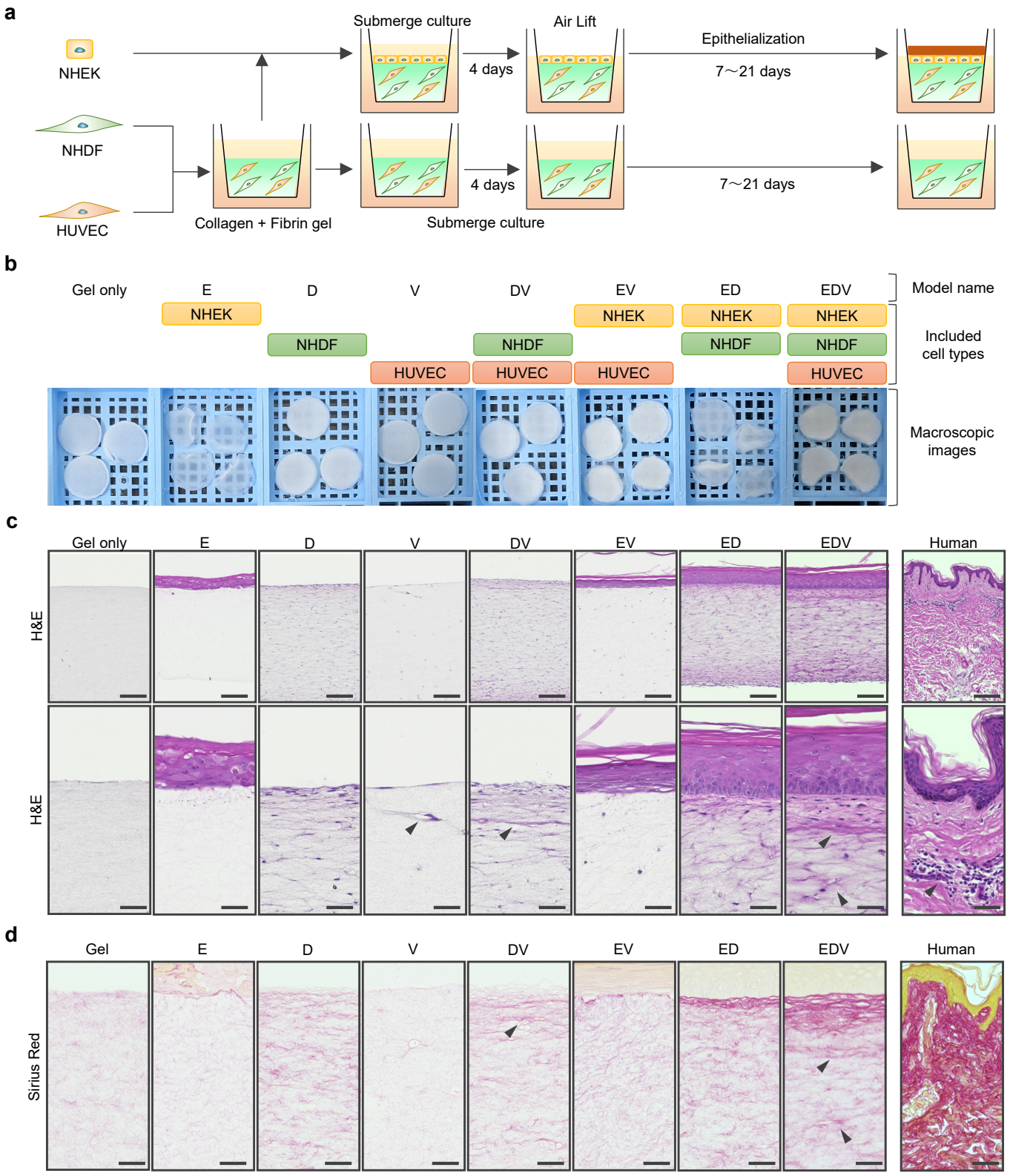

Figure 1 Tricellular communication regulates skin and vascular organization.
(a) Schematic of the construction method of HSEs. (b) Macroscopic images of the HSEs. Scale bar, 1 mm. (c) H&E-stained images of human skin and the HSEs at low (upper columns; scale bar, 200 μm) and high (lower columns; scale bar, 50 μm) magnification. The arrowheads indicate the endothelial tube. (d) Sirius red-stained images of human skin and the HSEs; scale bar, 50 μm.

S. Kimura et. al., Figure. 1

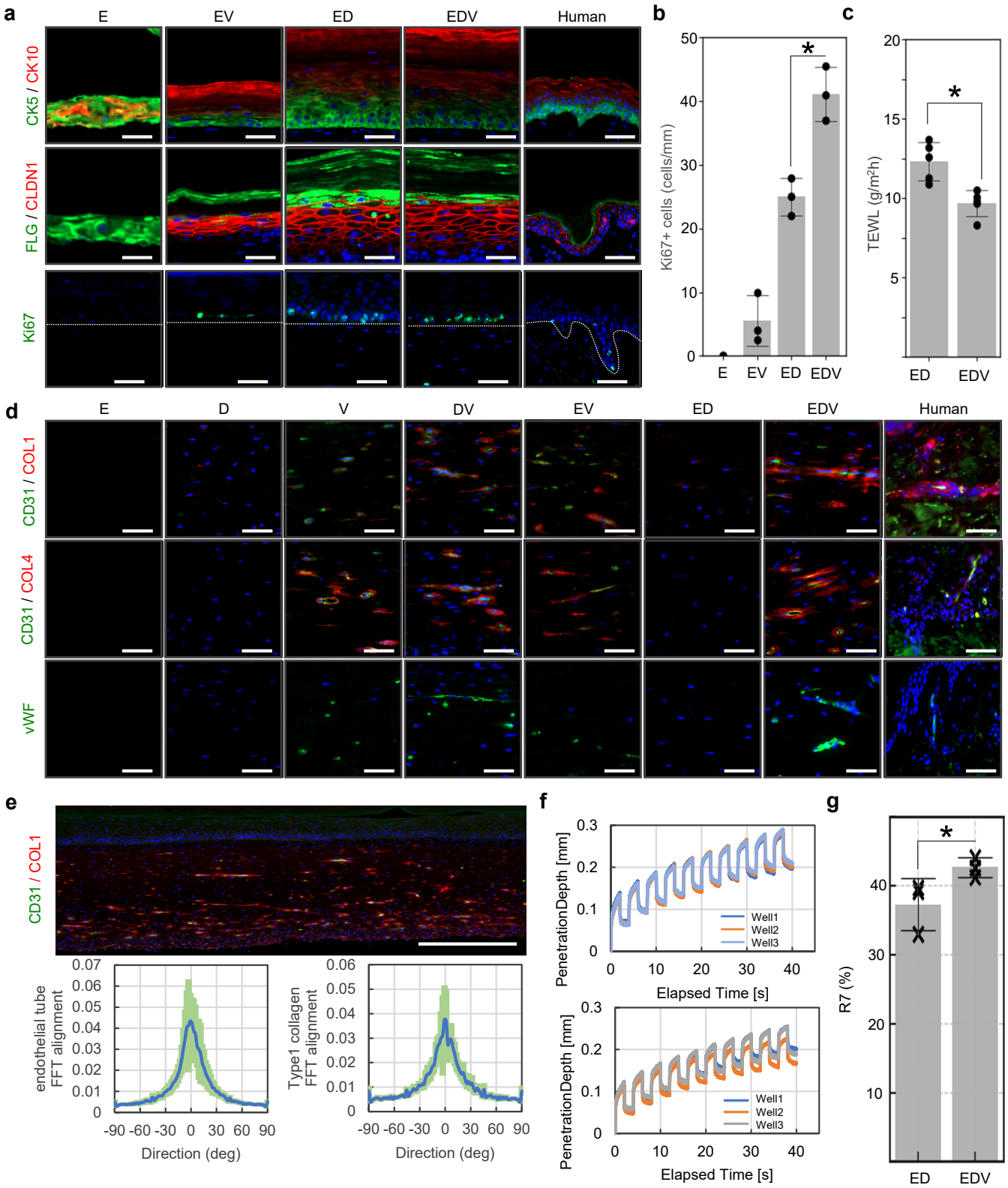

Figure 2 Tricellular communication enhances skin barrier function and elasticity by inducing self-organization.
(a) Immunohistochemical analyses of human skin and the HSEs for evaluating epithelialization. The dotted lines indicate the boundary between the epidermis and dermis. Scale bar, 50 μm. (b) Analysis of the Ki67-positive basal keratinocyte ratio in HSEs. *P < 0.001 (Dunnett's test following two-way analysis of variance). (c) TEWL analysis of the ED and EDV models *P < 0.05 (two-tailed Student's t–tests; error bars represent standard deviation). (d) Immunohistochemical analyses of human skin and HSEs for evaluating angiogenesis and dermal collagen synthesis. (e) Macroscopic image of CD31 and COL1 distribution (upper column) and FFT analysis (lower columns) of the alignment of CD31-positive endothelial tubes and COL1-positive type 1 collagen fibers in the EDV model. Scale bar, 500 μm. (f) Skin deformation curves of the ED (upper panel) and EDV models (lower panel). (g) Evaluation of R7 factors of the ED and EDV models. *P < 0.05 (two-tailed Student's t-tests; error bars represent standard deviation).

S. Kimura et. al., Figure. 2

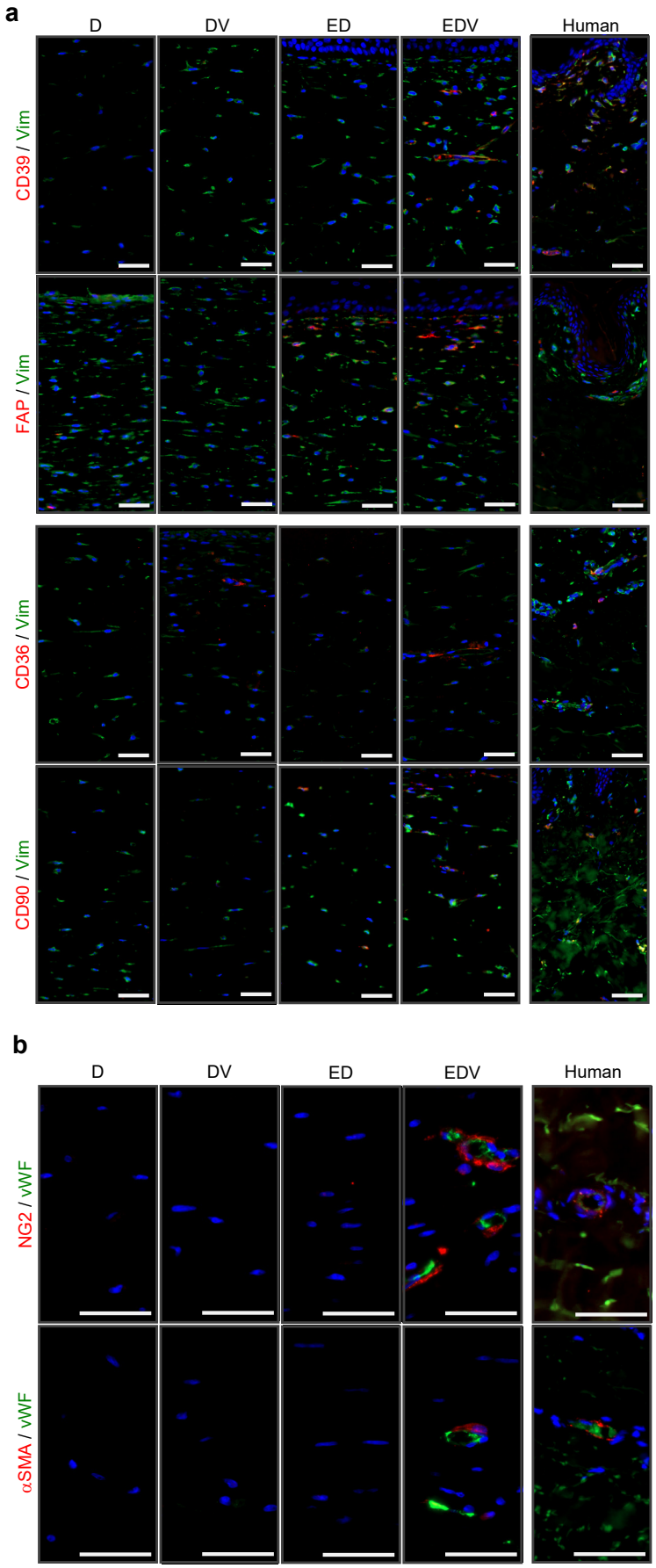

Figure 3. Immunohistological analysis of dermal mesenchymal cell distribution in the HSEs and human skin
(a) Immunohistochemical analyses of ED, EDV and human skin samples to evaluate the presence and distribution of dermal mesenchymal cell subpopulations. Scale bar, 50 μm. (b) Immunohistochemical analysis of pericyte distribution in ED, EDV, and human skin tissues. Scale bar, 50 μm.

S. Kimura et. al., Figure. 3

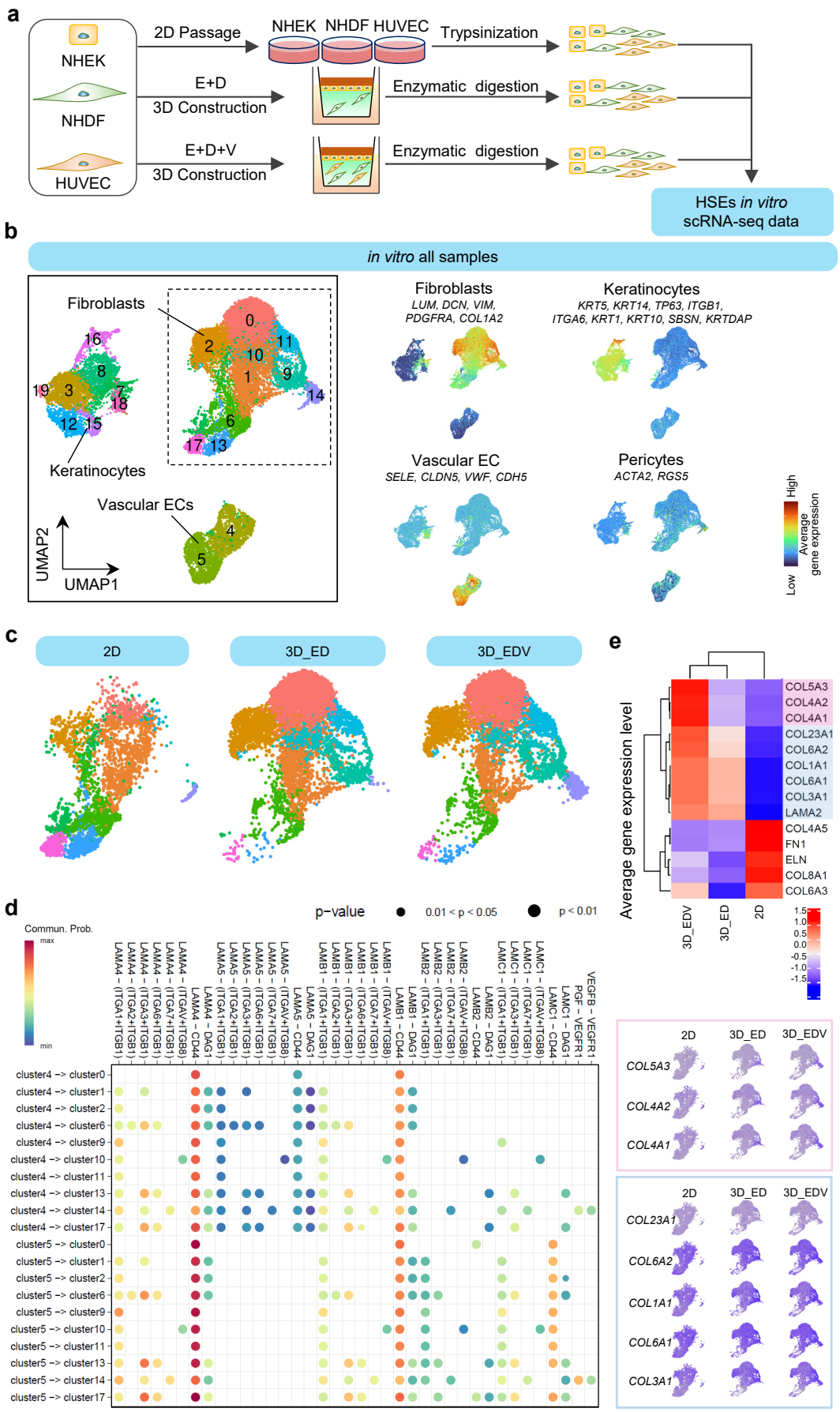

Figure 4. The 3D culture environment and cell-to-cell communication replicate dermal mesenchymal cell heterogeneity *in vitro*.
(a) Illustration of the workflow for sampling and analysis of the scRNA-seq data. (b) UMAP plot of the scRNA-seq data for *in vitro* HSEs; the average expression of four cell-type markers projected onto the UMAP plot for identifing cell populations. (c) Distribution of fibroblasts and pericytes under each of the three conditions. (d) Cellular communication from vascular endothelial cells (ECs; Clusters #4 and #5) to pericytes in Cluster #14 and fibroblasts in Cluster #9. (e) Heatmap showing the average expression of ECM-related genes across all fibroblasts under different conditions.

S. Kimura et. al., Figure. 4

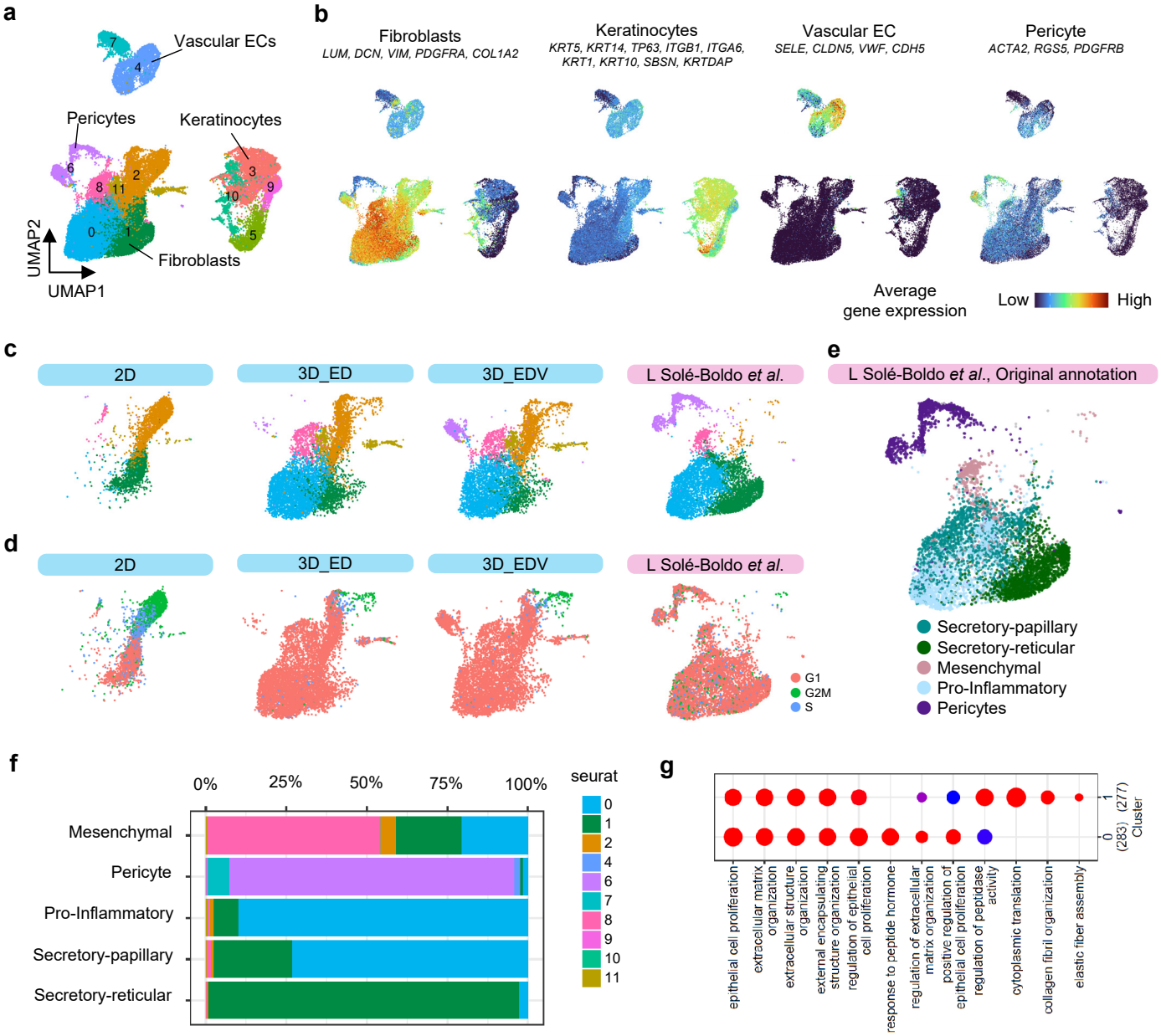

Figure 5 Biological significance of fibroblast heterogeneity in HSEs through integrated analysis of human scRNA-seq data.
(a) UMAP plot of the scRNA-seq data for integrating HSEs and *in vivo* skin data. (b) Average expression of established cell type markers was projected on the UMAP plot to identify cell populations. Red indicates maximum gene expression, whereas blue indicates low or no expression of a particular set of genes in log-normalized UMI counts. (c) UMAP plot integrating the scRNA-seq data of HSEs and *in vivo* skin, showing the distribution of fibroblasts and pericytes across the three *in vitro* and *in vivo* conditions. (d) Cell cycle status of fibroblasts under each condition. (e) UMAP plot showing the correspondence of the four fibroblast subpopulations and pericytes, as previously reported11. (f) Proportion of cells from each subpopulation as previously defined11 and their clustering into specific clusters, as shown in Fig. 4e. (g) Enriched GO terms in clusters #0' and #1'.

S. Kimura et. al., Figure. 5

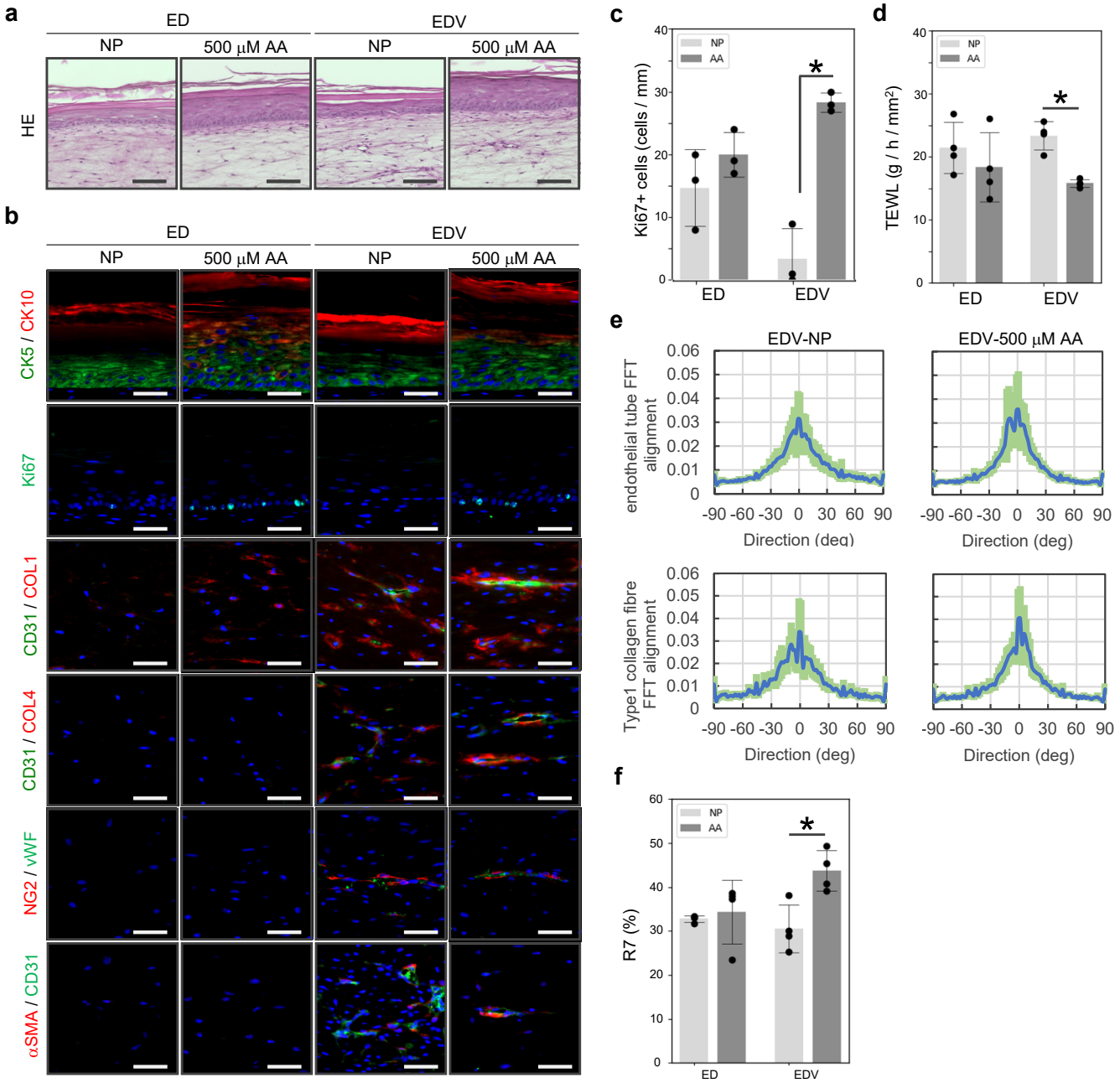

Figure 6 NP culture conditions in the HSEs induce a senescent phenotype, which is suppressed by AA.
(a) H&E-stained images of skin tissue organization induced by AA supplementation in the HSEs cultured under NP conditions. Scale bar, 100 μm. (b) Immunohistochemical analysis of the HSEs for visualizing the impact of NP conditions and ascorbic acid on re-epithelialization, dermal ECM synthesis, and angiogenesis. Scale bar, 50 μm. (c) Analysis of the Ki67-positive basal keratinocyte ratio in the HSEs. *P < 0.001 (two-tailed Student's t-tests; error bars represent standard deviation). (d) TEWL analysis of the ED and EDV models. *P < 0.001 (two-tailed Student's t-tests; error bars represent standard deviation). (e) A 2D-FFT analysis (lower columns) of the alignment of CD31-positive endothelial tubes and COL1-positive type 1 collagen fibers in the EDV model. (f) Evaluation of R7 factors of the ED and EDV models. *P < 0.01 (two-tailed Student's t-tests; error bars represent standard deviation).

S. Kimura et. al., Figure. 6

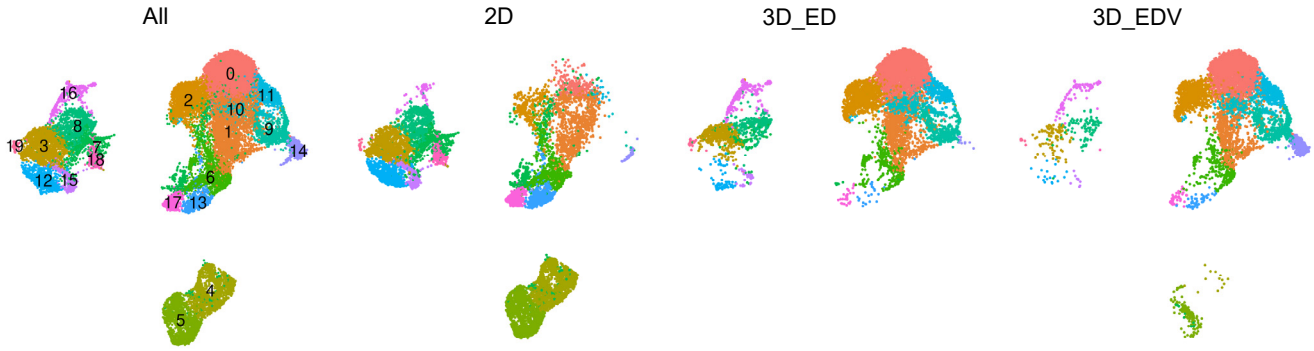

Supplementary Figure 1. scRNA-seq analysis of all in vitro samples.
UMAP plot of scRNA-seq for *in vitro* human skin data, and distribution of all cells under each of the three conditions (2D, 3D_ED, and 3D_EDV).

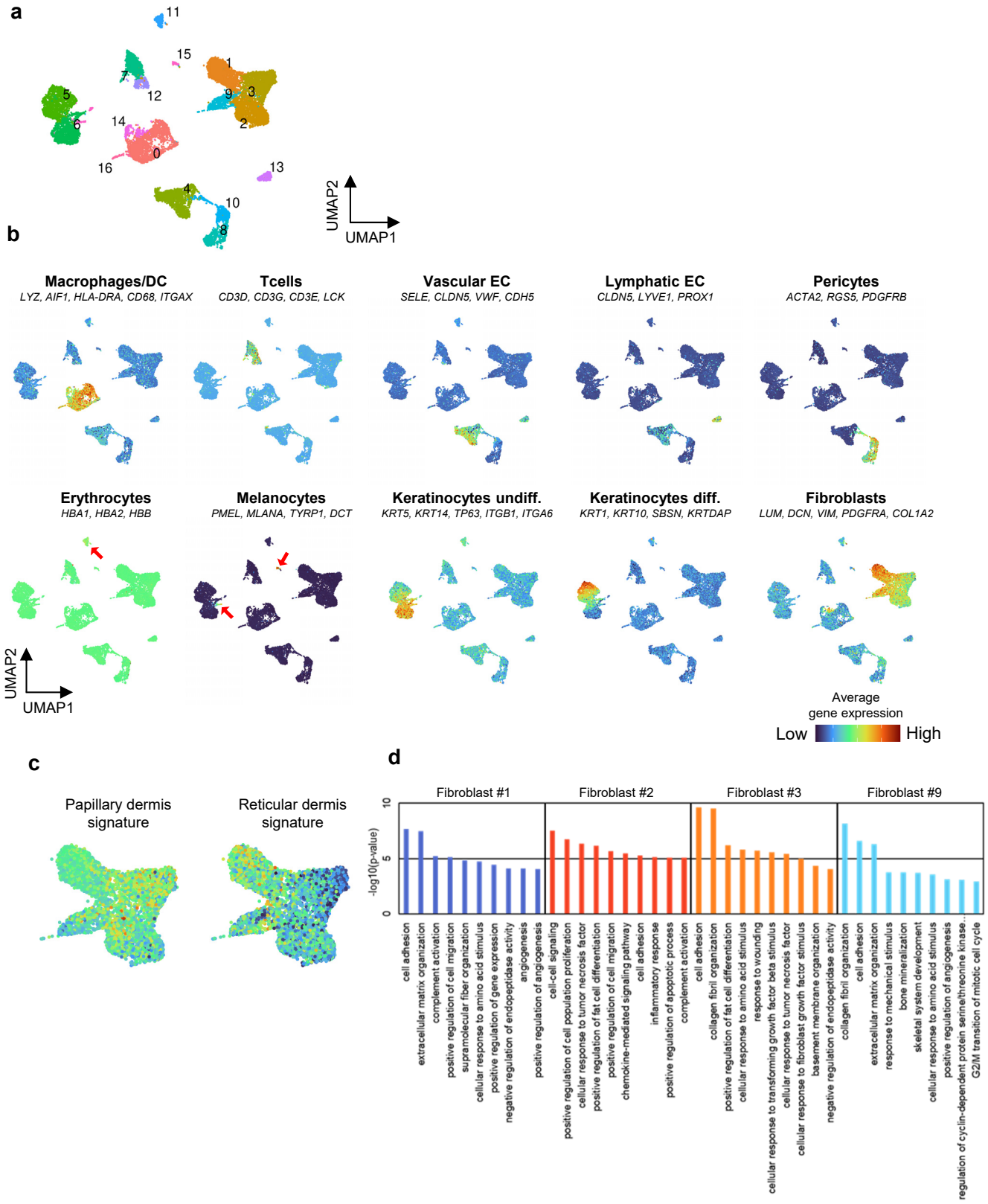

Supplementary Figure 2. Re-evaluation of *in vivo* samples through scRNA-seq.
(a) A UMAP plot presenting single-cell transcriptomic data from whole human skin samples (n = 5). Each point signifies a single cell, with coloration based on unsupervised clustering executed using Seurat. (b) Mean expression of genes forming the papillary and reticular gene signatures applied to predict the dermal localization of fibroblasts within the four clusters. (c) The 10 top significantly enriched GO terms within each fibroblast subpopulation, arranged by P-value (d) A UMAP plot featuring the average expression of previously established cell type markers for distinguishing cell populations. Red denotes maximum gene expression, whereas blue represents minimal or non-existent expression of a specific gene set in log-normalized UMI counts.

S. Kimura et. al., Supplementary Figure. 2